Thermal Stability and Photostability of Highly Confined Molecular Nanocomposites

Cindy Yueli Chen,[†] Haonan Wang,[‡] Ahmad Arabi Shamsabadi,[†] and Zahra Fakhraai[*,†]

[†]*Department of Chemistry, University of Pennsylvania, Philadelphia, Pennsylvania 19104, United States*

[‡]*Corning Research Center, Shanghai 201206, China*

E-mail: fakhraai@sas.upenn.edu

Abstract

Capillary rise infiltration of molecular glasses into self-assembled layers of rigid nanoparticles (NPs) can produce highly confined molecular nanocomposite films (MNCFs). Here, we investigate the thermal stability and photostability of MNCFs made by confining indomethacin glasses in silica NPs. We demonstrate increasing confinement decreases the rate of thermal degradation and increases the activation energy of degradation (up to ∼70 kJ/mol in 11 nm NPs, ∼ 3 nm pore size). Upon UV exposure under nitrogen, photodegradation is only observed at the near-surface region of MNCFs, with a thickness of one NP diameter. However, no further degradation is observed, even after prolonged UV exposure. The dramatically improved thermal stability and photostability of MNCFs can be attributed to the slower transport of reaction products, corresponding to the increased T_g (up to ∼ 30 K in 11 nm NPs). These findings demonstrate that extreme nanoconfinement can prolong the durability of molecular glasses in applications such as coatings and organic electronics.

Introduction

Extensive research has been conducted on polymer nanocomposites (PNCs), which show improved thermal,[1] mechanical,[2,3] optical,[3] and electrical characteristics.[4] The physical and chemical properties of PNCs can be altered by manipulating the interactions between the constituent polymer and nanomaterial building blocks, as well as controlling factors such as nanoparticle loading and aggregation geometry.[5,6] This approach enables the creation of multifunctional materials with tailored properties, suitable for various specialized applications such as photovoltaics, light emitting diodes, protective coatings, and membranes.[7–11] In general, the attainment of a desired attribute following the alteration of a PNC is complex. For example, numerous factors can increase the glass transition temperature (T_g) of PNCs, including nanomaterial and polymer types, nanofiller dispersion, nanofiller-polymer interactions, processing methods, and catalytic effects.[12–15] Similarly, multiple factors besides T_g variations can affect PNC's thermal stability, as different reaction pathways can be affected differently by the confinement and interfacial effect. Reports have shown slower thermal degradation with proper nanofiller loadings (≤ 18 wt%) using conventional fabrication methods, but increasing loading beyond this level does not provide additional benefits. These non-monotonic gains are attributed to the barriers to relaxation and the diffusion of degradation byproducts induced by nanofillers,[13,16–18] the catalytic effects of the nanofillers,[19–22] and their degree of aggregation.[14] Nanofiller aggregation at high loading can lead to a substantial propensity for thermal decomposition.[14] Photocatalytic degradation can also occur frequently in PNCs[19–22] and can pose significant problems when considering outdoor applications, such as light-harvesting devices and functional protective coatings. Strategies to limit these thermal degradation and photodegradation pathways are not broadly available and can highly depend on the chemical structure of the PNC.

Increasing T_g can be important in improving the thermal stability or photostability in systems where the reaction kinetics involve the diffusion of the reactants or products through the polymer matrix. Increasing T_g increases the structural relaxation time of the polymer

matrix, resulting in slower gas diffusion. In particular, polymers confined in nanoporous systems can show strong variations in their T_gs. For instance, T_gs of both polymers and small molecules when confined in controlled pore glass (CPG) and anodic aluminum oxide (AAO) can deviate from the bulk values due to both size confinement and interfacial effects, with several studies indicating the presence of two distinct T_g values.[23–26] However, these nanoporous structures have been observed to accelerate, rather than decelerate, thermal degradation in both polymers and some small molecules.[27,28] As such, accounting for the role of other variables such as interfacial interactions, effective pore size, pore geometry, etc., is also critical, but remains challenging, particularly in extreme nanoconfinement conditions.

Recently, a simple approach, called capillary-rise infiltration (CaRI), has been developed to prepare highly-loaded PNCs, with uniform dispersion on NPs.[29,30] In this method, a polymer-infiltrated nanocomposite film (PINF) is produced by annealing a bilayer consisting of a self-assembled NP film and a polymer film, at a temperature higher than T_g of the polymer. Under these conditions, capillary forces drive the polymer chains to infiltrate into the interstices of the NPs, placing the polymer under extreme degrees of nanoconfinement, without disturbing the NP packing. While decreasing the NP diameter increases the degree of confinement in these systems, the loading volume remains constant (63 vol% NP volume fraction). We have previously demonstrated that in weakly-interacting systems such as polystyrene (PS)/SiO_2 PINFs, increasing confinement can lead to dramatically increased T_g due to segmental-level constraints on relaxation dynamics (entropic effects).[31] Other properties such as viscosity, thermal stability, and mechanical properties have also been shown to be dramatically affected under these extreme nanoconfinement conditions.[32–35] In contrast to CPGs, the increased T_g in PINFs results in significant thermal stability, due to a dramatic slow-down of diffusion of the free radicals, oxygen, and reaction products. We have recently demonstrated that in PS/SiO_2 decreasing the NP diameter from 100 nm to 11 nm results in 55 kJ/mol and 70 kJ/mol increase in the activation energies for degradation at the film's center and film's surface, respectively. Furthermore, even in ambient conditions,

extreme nanoconfinement results in the suppression of the auto-acceleration and burning in PINFs.[32]

While traditional nanocomposites cannot be produced from molecular glasses due to the lack of chain connectivity, CaRI can be used to produce molecular nanocomposite films (MNCFs) with a similar degree of T_g increase (up to $\sim$ 30 K in 11 nm SiO_2 NPs) as previously measured in PINFs.[26] Such large increases in T_g had not been previously reported in other confined molecular glasses such as in CPG or AAO, indicating the important role of concave curvatures in self-assembled NP films in significantly restricting intra-molecular degrees of freedom.[26] The MNCFs properties can be further tailored through the Gibbs-Thomson effect,[36,37] by changing the interfacial interactions between NPs and the molecular glass. MNFCs thus emerge as a unique approach to improving functional properties and stability in molecular glasses, with potential impact in a broad range of applications, including small-molecule organic light-emitting diodes (SM-OLED), drug packaging,[38,39] stable UV absorbing materials and UV-resistant coatings in thin film solar cells, and cosmetic products.[20,40,41]

In this study, we utilize Spectroscopic Ellipsometry (SE) to investigate the effect of extreme nanoconfinement on the thermal stability and photostability of MNCFs using indomethacin (IMC) glass in silica NP films as a model system. SE is a nondestructive technique that is both reliable and effective in the measurement of optical properties,[42] film thickness,[43,44] surface coverage or homogeneity,[32] material porosity,[45,46] dielectric constant,[47,48] and conductivity[49] of materials in the visible and near-infrared spectral ranges. Upon UV irradiation or heat treatment in inert environments, such as under N_2 gas, the dominant degradation pathway for IMC is via decarboxylation, generating a single CO_2 molecule (Scheme 1).[50,51] As such, this is a good model system to investigate the interplay between T_g increase and the resulting slowdown of product gas diffusion on the composite stability under nanoconfinement. In IMC, both entropic (geometric confinement) and enthalpic (IMC interactions with SiO_2) effects can potentially lead to changes in molecular relaxation and,

thus, stability in nanoconfinement. We demonstrate that as the degree of nanoconfinement is increased by reducing the NP diameter below 25 nm, IMC liquid shows slower thermal degradation rates and increased activation energy for degradation. The degradation rate and the activation energy correlate with the increased T_g of IMC upon nanoconfinement. In the glass state, photodegradation under an inert environment is only observed at the surface region of the nanocomposite, which becomes thinner and degrades more slowly as the NP diameter is decreased. This is attributed to the dramatically improved kinetic stability of the confined IMC glass, which acts to dramatically suppress the product gas diffusion. The interplay between entropic (constrained molecule motion) and enthalpic (surface interaction) effects under extreme nanoconfinement leads to substantial thermal stability and photostability improvements of this nanocomposite material.

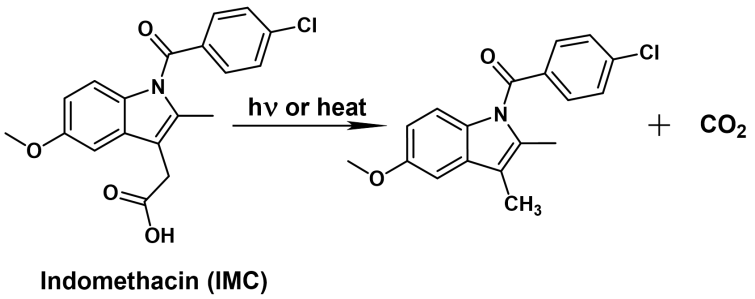

Indomethacin (IMC)

Scheme 1: As shown, thermal degradation or photodegradation of indomethacin (IMC) under inert environments such as N_2 gas occurs through decarboxylation.[50,51]

Materials and Methods

Sample preparation Prior to film deposition, one-sided-polished silicon wafers (Virginia Semiconductor $< 100 >$) were cut to approximately 1.5 cm $\times$ 1.5 cm squares. Indomethacin (IMC) (MilliporeSigma, M_W = 357.79 kg/mol) solutions were prepared by dissolving IMC in tetrahydrofuran (THF). Suspensions of silica nanoparticles (NPs) with various diameters, SiO_2 (11 nm) and SiO_2 (100 nm) (Nissan Chemical, 30-31 wt% suspension in IPA,) as well as SiO_2 (25 nm) (Sigma-Aldrich, Ludox TM-50, 50 wt% suspension in water), were diluted

with their respective solvents. The IMC solution and diluted NP suspensions were filtered using 0.2 or 0.45 µm PTFE syringe filters before use.

Preparation of IMC and IMC/SiO_2 nanocomposite films To prepare an IMC thin film, the IMC solution was spun cast (Laurell, WS-400BZ-6NPP/Lite spin-coater) onto a silicon wafer at a spin speed of 4000 - 6000 revolutions per minute (rpm). The film was then annealed under vacuum at 350 K for 30 minutes to remove the excess residual solvent. For an IMC nanocomposite film, a layer of SiO_2 NP (11, 25, or 100 nm diameter) was first spun cast onto a silicon wafer and sintered at 773 K for 30 minutes on a temperature-controlled stage (Linkam THMS600) to remove the solvent and chemically stabilize the NP layer. Upon cooling to room temperature, a layer of IMC was spun cast onto the NP layer to form a bilayer film, which was then annealed at 353 - 393 K to induce IMC infiltration. Infiltration was either performed on the Linkam stage under N_2 for *in situ* monitoring or in a vacuum oven. The thickness of either IMC or NP films was adjusted by changing the spin speed and concentration of the prepared solution/suspension. For thermal degradation measurements, each MNCF consisted of a $\sim$ 200 nm nanocomposite layer with a $\sim$ 20 nm IMC top layer after infiltration. For photodegradation measurements, the thickness of the nanocomposite layer was either $\sim$ 200 or $\sim$ 400 nm, and a top IMC layer with a thickness of $\leq$ 5 nm after infiltration.

Spectroscopic Ellipsometry (SE) Measurements

T_g **measurements** Either IMC or IMC/SiO_2 films were first mounted onto the Linkam temperature-controlled stage that was attached to a spectroscopic ellipsometer (SE, M-2000 V, J.A. Woollam). The Linkam stage was sealed inside a custom aluminum cap with an optical adapter at a 70° angle of incidence to facilitate *in situ* SE measurement under a controlled environment.[52] The sample stage was depressurized by a vacuum pump and re-filled with dry N_2 gas. The raw SE data, $\Psi(\lambda)$ and $\Delta(\lambda)$, were measured in the spectroscopic

range of 600 nm $< \lambda <$ 1600 nm and were fit to a model consisting of either one (pure IMC films) or two (films consisting the IMC nanocomposite layers and the IMC top layers) transparent uniform Cauchy layers on top of a silicon substrate with a 1 nm native oxide (see Figure S4 for more details). The real (n) and imaginary (k) parts of the index of refraction for each Cauchy layer were modeled as $n(\lambda) = A + B/\lambda^2$ and $k(\lambda) = 0$, respectively. A and B are fitting parameters along with the film thickness h. The optical constants of the Si substrate and the native oxide layer were obtained based on the literature values.[53] When necessary, after the initial fitting, some variables, such as the nanocomposite layer thickness, were kept constant during *in situ* SE measurements throughout the thermal cycle to avoid over-fitting insensitive parameters. The samples were subject to heating/cooling ramps (example shown in Figure S1), and *in situ* SE data were collected with a sampling rate of 1 s, with high accuracy zone averaging. The thickness and refractive index of the IMC top layer and the refractive index of the nanocomposite layer were modeled to fit the raw SE data while keeping the nanocomposite layer thickness constant to avoid overfitting. The infiltration process was completed during the first heating ramp. T_g of each layer was measured upon subsequent cooling at a cooling rate of 10 K/min (Figure S1).

Thermal degradation measurements The same experimental setup was used to monitor the thermal degradation of nanocomposite layers under dry N_2. For each measurement, the heating rate was set at 64 K/min to reach the target temperature, in the temperature range of 453 K - 473 K, where the sample was held isothermally, and the thermal degradation was monitored *in situ* using SE, with a sampling rate of 1 s using high accuracy zone averaging. The SE data were fitted to a Cauchy (top IMC layer) and a linearly-graded Cauchy (bottom IMC nanocomposite layer) bilayer model (examples shown in Figure S4 of the SI). In the measurement, the refractive index of the top IMC layer was held constant as the film thickness was less than 20 nm, and the instrument is insensitive to small changes in this layer during degradation. In addition, the thickness of the nanocomposite layer was

also fixed, as the NP layer is rigid and does not change its thickness. For more details on the choice of model and fitting procedures, see Supporting Information and Figure S4).

Photodegradation measurements A UV lamp with a wavelength range of 254/365 nm (Analytikjena® UVP 95-0007-05 Model UVGL-58) was used as the light source to induce photodegradation of IMC. During measurement, an IMC or IMC/SiO_2 was placed in a custom SE stage with a cap and optical adapter, which allowed the SE incident light to enter and exit at a 70° incident angle and another window above the sample to allow the UV light to pass through at normal incidence angle. Each sample was illuminated with UV light placed at normal incidence with a distance of $\sim$ 30 mm away. Illumination started after at least 30 min of consistent dry N_2 flow in the chamber to establish a baseline and ensure dry conditions. The *in situ* SE measurement was performed throughout the process at a sampling rate of 10 s and with high accuracy zone averaging. $t = 0$ denotes the beginning of the UV exposure. The raw SE data were fit to a one-layer Cauchy model on top of a silicon substrate with a 1 nm native oxide (linear-graded or exponentially-graded refractive index, more details in SI and Figure S8). All key parameters were fitted, except for the film thickness, to avoid overfitting, as the thickness of silica NP or nanocomposite layer is not expected to change upon UV illumination.

UV absorption analysis The absorption spectra of IMC films with various thicknesses and IMC nanocomposite films (Figure S14) were obtained using a UV-Vis spectrophotometer (Varian Cary 6000i). The IMC and nanocomposite films were prepared as detailed above but with quartz discs as substrates (Chemglass Life Sciences, 1-inch Diameter, 1/16-inch Thick) instead of silicon wafers. The IMC spectra were recorded in the wavelength range of 200 – 500 nm, referenced to a blank quartz disc.

Results and Discussion

Glass transition temperature of confined IMC IMC/SiO_2 MNCFs were prepared using capillary rise infiltration (CaRI).[29,31,32] More details can be found in **Materials and Methods**. The degree of confinement was tuned by varying the NP diameters between 11 - 100 nm. Previous studies have shown that the average pore sizes in these systems can range between 3 - 33 nm, roughly 1/3, or the NP diameter, with a broad distribution of pore sizes and shapes.[45,54] Spectroscopic ellipsometry (SE) was used to monitor the completion of the IMC infiltration process. The resulting MNCFs typically contained a $\sim$ 200 nm nanocomposite layer at the bottom and a thin layer of IMC on top with a 20 - 30 nm thickness. The volume fraction (ϕ) of IMC inside the nanocomposite layer was determined from the refractive indices of pure NP films, a pure IMC film, and the nanocomposite layer, measured separately by SE (more details in SI, values shown in Table S1). The average volume fraction was measured to be $\phi \sim 30 \pm 5$ % (Table S1), consistent with near complete filling of the pores, as the maximum limit in randomly closed packed films of monodispersed NPs is 37 %.[55]

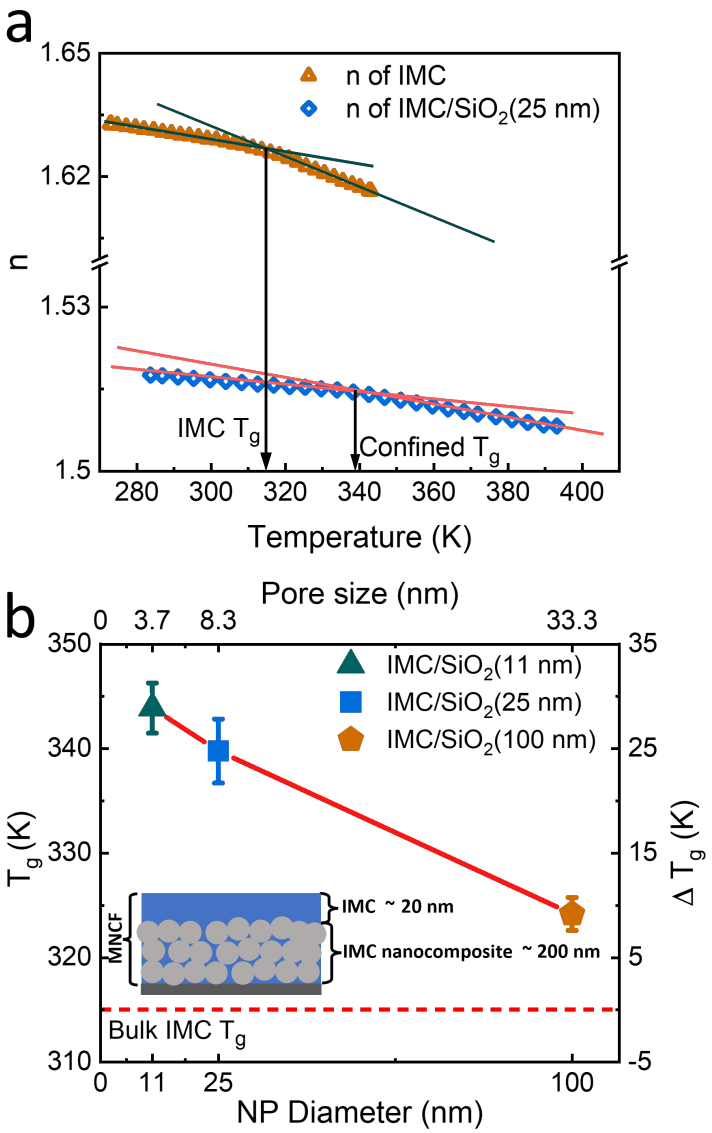

Figure 1: (a) Refractive index (n) measured at $\lambda = 632.8$ nm, vs. temperature for a bulk IMC film ($\sim$ 350 nm, orange symbols) and the nanocomposite layer ($\sim$ 200 nm, blue symbols) of an IMC/SiO_2(25 nm) film, both made on silicon substrates, measured upon cooling at a rate of 10 K/min. The solid green and red lines are linear fits to the glass and supercooled liquid regions for the IMC film and the nanocomposite layer, respectively. T_g values were determined as the cross-sections of these regions, as shown by the corresponding black arrows, and were measured to be T_g(IMC) $= 315 \pm 2$ K and T_g(confined) $= 339 \pm 3$ K, respectively. (b) T_g vs. NP diameter for $\sim$ 200 nm nanocomposite layers of IMC/SiO_2 films with a $\sim$ 20 nm IMC top layer as schematically shown in the inset. The red dashed line shows the bulk T_g value of IMC.

The T_g of the nanocomposite layers and bulk IMC films were also measured by *in situ*

SE at a cooling rate of 10 K/min (Figure S1).[56,57] Figure 1a shows an example of the measured refractive indices of a bulk $\sim$ 350 nm IMC film and a fully infiltrated $\sim$ 200 nm nanocomposite layer (IMC/SiO_2(25 nm), $\sim$ 8 nm pore size), as a function of temperature. The T_g values were determined to be T_g(IMC) = 315 $\pm$ 2 K and T_g(confined) = 339 $\pm$ 3 K, respectively (Figure 1a). As shown in Figure 1b, the nanocomposite T_g is increased upon increasing the degree of confinement. In the most confined system with 11 nm SiO_2 NPs ($\sim$ 3 nm pores), a T_g increase of $\Delta T_g = 29 \pm 2$ K is observed compared to the bulk IMC T_g. This large increase in T_g is comparable with values reported in PINFs[31,33] and another molecular nanocomposites system[26] with weak interfacial interactions with SiO_2 surface. In those systems, the effect was mostly attributed to increasing barriers for relaxation and improved kinetics stability of IMC glass under extreme nanoconfinement.[26,32,33] However, a slight increase in the breadth of the T_g transition (from $\Delta T_g = 20$ K to $\Delta T_g = 27$ K) is also observed in IMC MNCFs as the pore diameter is decreased (Figure S2), which was not seen previously in systems with weak interfacial interactions. The increased breadth of transition can be attributed to interfacial effects due to the hydrogen bonding of IMC to the silica surface,[15,58,59] further slowing down the relaxation dynamics.

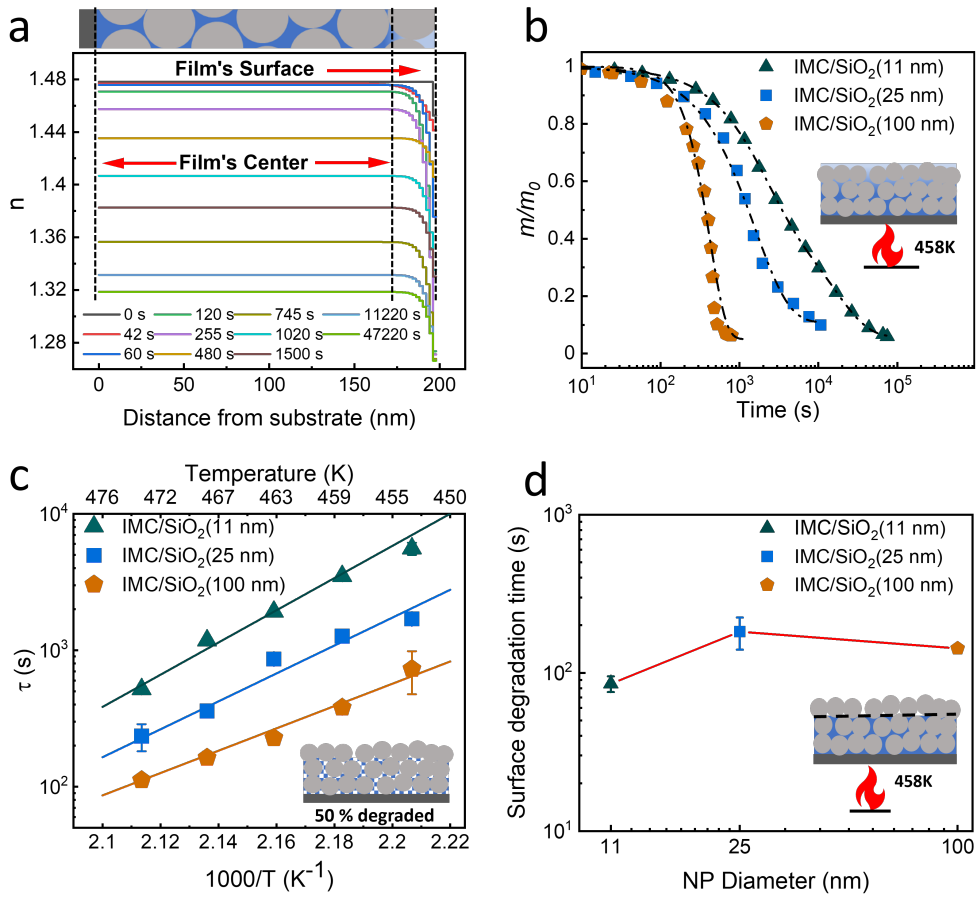

Figure 2: (a) Refractive index as a function of distance from the substrate of a $\sim$ 200 nm layer of IMC/SiO_2(25 nm) at various times during isothermal degradation at 458 K under N_2. t = 0 s is the time when the top IMC layer is completely degraded, exposing the nanocomposite surface (Figure S3 of SI). The top sketch indicates the position of the substrate, a depth equal to the NP diameter (25 nm), and the nanocomposite surface with dotted lines, separating the layer's surface and center regions (indicated by red arrows). (b) Normalized mass loss (m/m_0) of the nanocomposite layer of various NP diameters during isothermal degradation at 458 K under N_2 (schematically shown in the inset). The dashed lines are fitted as detailed in SI. (c) Thermal decomposition time at 50% mass loss ($m/m_0 = 0.5$, schematically shown in the inset) vs. 1000/T of nanocomposite layers of various diameters. (d) Thermal degradation time at the surface of $\sim$ 200 nm IMC nanocomposite layers during isothermal degradation at 458 K. Error bars represent the standard error of at least three samples.

Isothermal degradation of IMC nanocomposites Isothermal degradation measurements were also carried using *in situ* SE under N_2. As detailed in the **Materials and Methods** section, these measurements were performed at temperatures well above the highest measured T_g ($T_{anneal} > T_g(confined) + 100$ K), to ensure that the films were at equi-

librium by the time the target degradation temperature was reached. To gain insight into the degradation details, the data for the nanocomposite layer were fitted by various Cauchy models, including uniform, linearly-graded, and exponentially-graded refractive index (Details in **Materials and Methods** section and SI). The mean square error (MSE) of fitting was used to determine the most appropriate model of the layer's optical properties. Both the linearly-graded and exponentially-graded refractive index models exhibited decreased MSE values compared to the homogeneous model (Figure S4). Both models also suggested that the properties of the nanocomposite layer remained constant until the top IMC layer underwent full degradation (Figure S3). This time was denoted as $t = 0$ s for the nanocomposite layer degradation, after which degradation proceeded inhomogeneously throughout the film, with a non-monotonically changing degree of inhomogeneity during degradation (Figure S5). Figure 2a shows the index of refraction as a function of distance from the substrate at various annealing times, according to the exponentially-graded index model (lowest MSE in fitting). As seen in this Figure, at all time depth, the refractive index of the regions near the surface IMC/SiO_2(25 nm) at $\sim$ 200 nm (and IMC/SiO_2(100 nm) shown in Figure S6) is slightly lower than that in the film center (which is nearly constant below a certain point), suggesting that the top layer has faster degradation and is removed, before the film center degradation starts, resulting in inhomogeneous refractive index. The faster degradation rate of the free surface region is consistent with our previous report in which similar differences in the rate of surface and bulk degradation were observed in PS-infiltrated nanocomposite films (PS/SiO_2).[32] In MNCFs with various diameters, the thickness of the surface region with faster degradation roughly corresponds to the NP diameter ($\sim$ 25 nm in Figure 2a. Data for $\sim$ 11 nm and $\sim$ 100 nm shown in Figure S6). We note that while at the same temperature, the degradation time at the surface is similar in MNCFs with various diameters (Figure 2d), as the NP diameter is decreased, the total amount of degraded mass is smaller in smaller NPs, due to the smaller thickness of the surface region.

Aside from the surface region, the degradation of the film center is seen as the change

in the baseline values of the index of refraction (flat regions in Figure 2a) as a function of time, which proceeds more slowly than the surface region. The mass loss, calculated based on the change in the index of refraction of this region, has a uniform rate throughout the film. Figure 2b shows the calculated mass at the nanocomposite layer's center with time for nanocomposite layers of various diameters. It is seen that the degradation rate is slower as the degree of confinement is increased (decreasing NP diameter). This trend holds at various annealing temperatures 453 K$\leq$ T_{anneal} $\leq$ 473 K, as depicted in Figure 2c (Upper axis). Figure 2c shows the Arrhenius plot of degradation time (τ), determined at 50% mass loss ($m/m_0 = 0.5$), as a function of 1000/T. This plot demonstrates that the degradation rate at the center of the nanocomposite layer follows an Arrhenius relationship. Based on the slopes of the Arrhenius lines, the calculated activation energies for degradation at the composite layer center are 156 ± 16 kJ/mol, 196 ± 13 kJ/mol, and 226 ± 11 kJ/mol for IMC/SiO_2(100 nm), IMC/SiO_2(25 nm) and IMC/SiO_2(11nm), respectively. As such, the barrier for degradation is higher for IMC confined in 11 nm NPs ($\sim$ 3 nm pores) compared to 100 nm NPs ($\sim$ 30 nm pores) by $\sim 70 \pm 27$ kJ/mol.

Previous studies showed an increased activation energy of $\sim$ 55 kJ/mol for PS(8kg/mol) degradation under similar conditions 102 ± 13 kJ/mol (PS/SiO_2(100nm)), 129 ± 5 kJ/mol (PS/SiO_2(25nm)), and 157 ± 16 kJ/mol (PS/SiO_2(11nm)), with a total change of $\sim 55 \pm 15$ kJ/mol in the degradation barrier.[32] Since PS weakly interacts with the silica surface, the increased barrier for degradation was attributed to the loss of configurational degrees of freedom under extreme nanoconfinement[26] and the resulting T_g increase in these films (Δ T_g $\sim$ 50 K in 11 nm NPs). In the IMC MNCFs, the change in the barrier for degradation upon confinement is measured to be slightly larger. Given the increased breadth of the T_g transition in IMC MNCFs due to interfacial effects, it is likely that the hydrogen bonding of IMC to the silica surface[58,59] also contributes to the observed increase in degradation barriers. In contrast, the larger T_g change in PS compared to both IMC and previous molecular nanocomposites[26] is likely due to additional constraints on the polymer chain.

Another possible explanation is that the various stages of IMC degradation are affected by the confinement differently, as the confined IMC appears to have a two-step decay process (double exponential fits as detailed in SI), while the glass confined in 100 nm NPs shows a faster compressed exponential decay. It is possible that the first degradation step is not captured in 100 nm NPs, due to its rapid degradation. Similarly, in IMC/SiO_2(25 nm) films, at higher annealing temperatures, only one degradation process is captured (Figure S7), meaning that the two processes have different temperature-dependent degradation rates, that are affected differently by nanoconfinement.

Under inert environments such as the N_2 gas used here, the first decay step for IMC is degradation by the cleavage of the indole structure to produce CO_2 (Scheme 1).[50,60] As the T_g is increased and the dynamics of the glass are slowed, increasing the viscosity, the layer acts as a gas transport barrier with a reduced rate of diffusion of CO_2. The slow diffusion then results in a slower degradation rate and higher thermal stability at the layer's center, while at the surface, CO_2 can readily evaporate. This mechanism also explains why the first layer of the nanocomposite surface, has a faster rate of degradation than the rest of the film. It is notable that at the film surface, the degradation time is relativity independent of the NP size (Figure 2d), while the thickness of the degraded layer decreases as the NP diameter is decreased (roughly equal to the NP diameter as shown in Figure S6), meaning that less amount of material is lost due to surface degradation, improving the overall thermal stability of the MNCF.

Photodegradation of IMC molecular nanocomposites Photodegradation of IMC nanocomposite layers (with ≤ 5 nm top IMC layer) was investigated using *in situ* SE purged with N_2. The samples were illuminated with 254 nm UV at normal incidence at a distance of 30 mm from the surface. More details can be found in the **Materials and Methods** section. Similar to the thermal degradation, various models were examined for fitting the SE data with the exponentially-graded model yielding the lowest MSE values (Figure S8). When

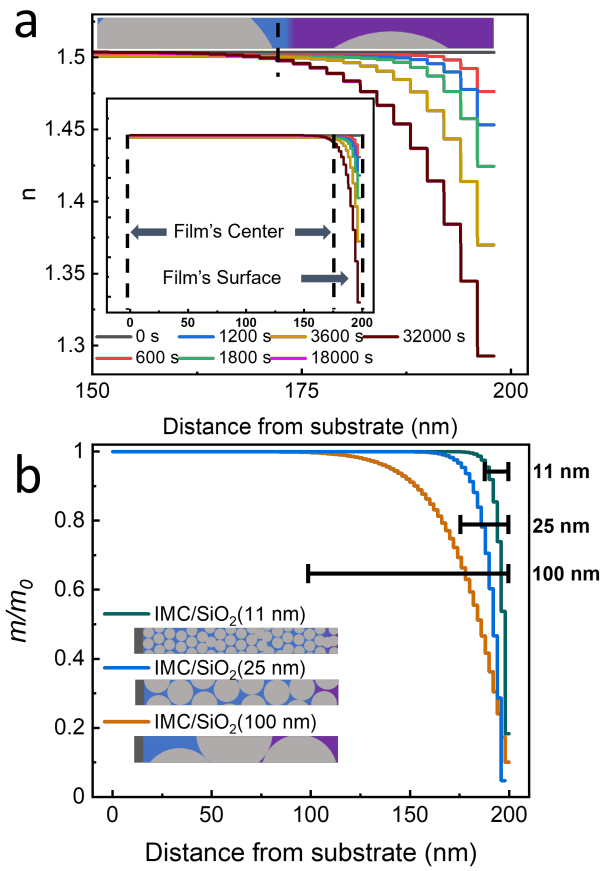

Figure 3: (a) Refractive index n as a function of distance from the substrate in the surface region (150 - 200 nm) of a $\sim$ 200 nm IMC/SiO_2(25 nm) nanocomposite layer at various times during UV irradiation (254 nm) under N_2. The inset shows the corresponding data throughout the entire film. The schematic on top shows a slice of the film with the surface region (purple, thickness of $\sim$ 1 NP diameter) marked by a dashed line. (b) Mass loss as a function of distance from the substrate for $\sim$ 200 nm nanocomposite layers prepared from various NP diameters, after 10 hr of UV irradiation (254 nm) under N_2. Black bars indicate the thickness of the surface region in each film, corresponding to one NP diameter. The inset schematically shows slices of nanocomposite layers of various diameters with their surface regions indicated with purple color.

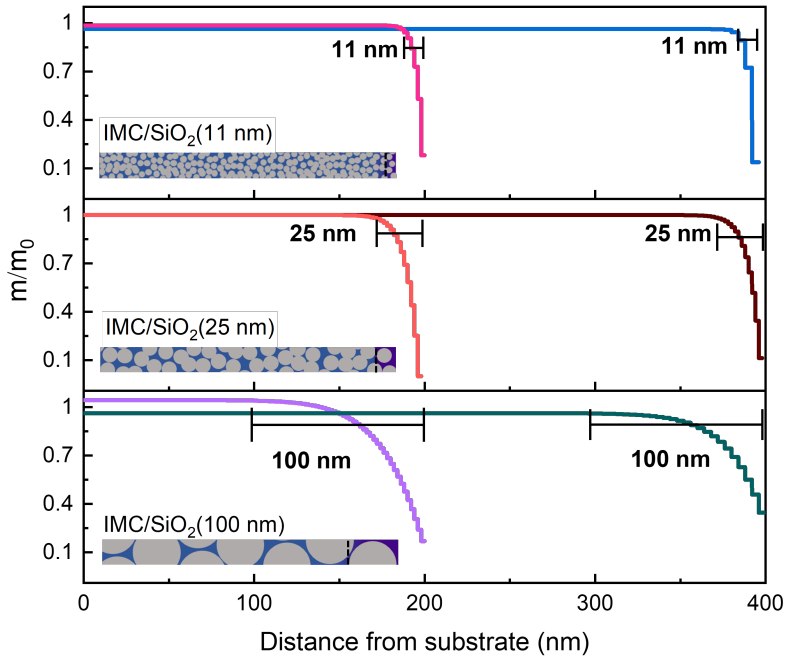

Figure 4: Mass loss as a function of distance from the substrate after 10 h of UV irradiation under N_2 for ∼200 nm and ∼400 nm IMC nanocomposite films prepared using various diameters of NPs. Black bars show the surface region of each film, with the size of one NP diameter in each plot.

a linearly-graded model was assumed, the surface roughness of MNFC exhibited minimal variation before and after photodegradation (Figure S13). In contrast, the inhomogeneity of the index of refraction was observed to increase in all MNCFs (Figure S9), with a negative value (negative % inhomogeneity), meaning that similar to the thermal degradation case, degradation started at the film's surface. Similarly, a larger inhomogeneity was observed in films with larger NP diameters, indicating that a larger portion of the surface region was degraded (Figure S9). However, in contrast to the thermal degradation measurements, where inhomogeneity eventually decreased upon degradation at the film's center, during photodegradation, the %inhomogeneity plateaued and did not change even after prolonged exposure to UV (Figure S9), indicating that the film center did not degrade within the experimental window studied here (up to 10 hours of exposure time).

The details of the surface degradation of IMC upon UV irradiation are clearer when the more reliable exponentially-graded model is used to fit the data with lower MSE values.

Figure 3a shows the refractive index of a $\sim$ 200 nm IMC/SiO_2(25 nm) film at various UV (254 nm) irradiation times using the exponentially graded model. As seen in this figure, the refractive index of the layer's surface decreases with longer irradiation time. In contrast, even after 32000 sec of exposure, the refractive index of the nanocomposite layer's center remains approximately constant within the experimental error. Significantly, while the rate of surface degradation appears to be independent of the NP diameter with a single decay function (Figure S11), the depth at which degradation is observed is roughly equal to the NP diameter in each MNCF film (Figure 3b and Figure S10). As such, when the NP diameter is decreased, a larger portion of the nanocomposite layer ($\sim$ 94.5% in 11 nm NPs) remains completely protected against photodegradation. In addition, when the film thickness is increased from $\sim$ 200 nm and $\sim$ 400 nm (Figure 4), the thickness of the degraded surface region remains constant; roughly equal to the layers corresponding NP diameter. As such, an even larger portion of the film is now extremely resistant to photodegradation ($\sim$ 97.25% in $\sim$ 400 nm MNCFs made of 11 nm NPs), showing no indication of degradation even after 10-hour UV irradiation (Figure 4). The interior of films made with 11 nm silica particles is fully UV-protected after the top layer degradation. In contrast, the degradation rate of pure IMC films with thicknesses less than 145 nm (with equivalent IMC mass as a 480 nm MNCF) is independent of their film thickness (Figure S14). In the solid state and under inert gas, upon UV illumination, IMC does not fully degrade small gaseous products. Instead, it loses its CO_2 throughout the thickness of the film. If IMC fully converted to 100% decarboxylated products, without any additional secondary reactions, a total mass loss of 12.5% total is expected, which should be measurable as a similar percent thickness change, as reported previously in IMC stable glass.[51] The data in Figure S12 shows that under the experimental conditions used in this study, 92% of the thin IMC film mass is retained ($\sim$ 8% mass loss), which is slightly less than complete degradation, indicating that IMC remains partially undegraded, even in thin films.

In MNCFs, the rigid structure of the NPs prevents the film thickness change upon mass

loss, and only the surface layer can degrade by reducing its volume. Interestingly, the surface degradation rate in MNCFs is similar to that of thin films, as seen in the rate of change in % inhomogeneity in Figure S9, indirectly corroborating this mechanism for surface decay.

In the absence of volume change, the degradation of the film center should be seen as a change in the film's index of refraction. An $\sim 8\%$ CO_2 mass loss throughout the film should result in a value of index of refraction of approximately 1.47 for IMC/SiO_2(11 nm), 1.48 for IMC/SiO_2(25 nm) (data in Figure 3a) or 1.50 for IMC/SiO_2(100 nm) at the film center, which would have been measurable by SE. However, the data in Figures 3a&b and 4 do not show any such change in the film center even after prolonged exposure.

The effect of UV penetration depth in these observations should also be considered due to the high UV absorbance of IMC (Figure S14). For example, in pure IMC film with a thickness > 300 nm, UV degradation slows down due to decreased UV intensity deeper into the film (Figure S12). As shown in Figures S14a and S14c, SiO_2 does not have significant absorbance in the wavelength range of interest. As such the UV extinction in MNCFs is primarily due to their IMC content, meaning that 200 nm and 400 nm MNCFs have similar UV absorbance values as 70 nm and 140 nm pure IMC films, respectively (Figure S12). Furthermore, in films of each thickness, the relative mass of IMC to silica is the same of NPs of various diameters, but their mass loss decreases with the NP diameter and is seen only at their surfaces. As such, UV light penetration cannot explain the protective role of confinement in the UV stability of MNCFs.

The role of rigidity in improved photostability While thermal stability and photostability are both improved by increasing the degree of confinement, they show notably different outcomes. In thermal degradation, once decarboxylation is complete, the material continues to break down until full degradation. In contrast, in photodegradation under inert conditions (N_2 gas here), only decarboxylation is seen in the time scales of these experiments, even in pure IMC films. This is likely because, in the glassy state, further degradation requires a

rearrangement of molecules, while decarboxylation is a local, molecular-level process.

Confinement appears to affect these processes differently. In thermal degradation, IMC is in a liquid state and can quickly equilibrate. As the degradation proceeds beyond the surface layer and the filling ratio of the composite is reduced, capillary driving forces move the molecules towards the narrowest pores, resulting in an underfilled structure with more confined states as previously detailed.[31,32] The increased spatial confinement as well as stronger IMC interactions with NP walls, result in a stronger slowdown of dynamics with increasing confinement. As such the degradation barrier dramatically increases as the NP diameter is decreased (Figure 2c). A simple Arrhenius extrapolation of these degradation times to room temperature would suggest that the photodegradation rate in IMC/SiO_2(11 nm) MNCFs should be at least $\sim$ 5 decades slower than in IMC/SiO_2(100 nm).

To obtain the hypothetical experimental time needed to observe photodegradation in MNCFs, the surface degradation times in thermal degradation and photodegradation can be compared. In both processes, degradation starts at the layer's surface, where the gaseous degradation products such as CO_2 can readily evaporate. While the thickness of the exposed surface layer decreases with the NP diameter, in both cases (Figures 2d and S11) the surface degradation rate remains bulk-like and unaffected by confinement. In thermal degradation at 458 K, the degradation time of the un-confined molecules at the IMC/SiO_2(100 nm) film surface is approximately $\sim$150 s (Figure 2d). The thermal degradation time of the film's center at this temperature is measured to be $\sim$650 s (more details in SI and Figure S5), indicating a moderate degree of confinement, which is also corroborated by the small change in the film's T_g (Figure 1b). Using a similar comparison, the midpoint of decarboxylation for IMC thin films and the surface of IMC/SiO_2(100 nm) films are both approximately $\sim$3000 s (Figure S12) and $\sim$3000 s (Figure S11), respectively. Given the moderate degree confinement of the IMC/SiO_2(100 nm) film, one would expect to observe photodegradation in the film center within $\sim$ 13000 s of photodegradation, which is within the experimental window of measurements. Given that no degradation is observed even after $\sim$ 60000 s of

UV irradiation (Figure S10c), the lower bound value of photostability in IMC/SiO_2(100 nm) film center is at least $\sim$ 4.6 times that of its surface. Remarkably, given that the relaxation dynamics in IMC/SiO_2(11 nm) are expected to be at least $\sim$ 5 decades slower than IMC/SiO_2(100 nm), based on the extrapolated thermal degradation times, the decarboxylation of the IMC/SiO_2(11 nm) film center should take more than 10^6 s (> 11 days).

This value is again just a lower bound for photodegradation in these systems, as no measurable change in the index of refraction was observed in the film center even in IMC/SiO_2(100 nm) MNCFs. This is likely because the rigid scaffold of the NPs, even when relatively large NPs are used, prevents a volume change in the IMC material. The resulting tensile stress would disfavor a reduction in film density, further increasing the barriers for degradation in the glass state, while these effects do not play a role in the liquid state where the liquid can readily relax.

To further highlight the remarkable UV protection provided by the rigid NP scaffold, the results can be compared with previous studies in highly stable glasses (SGs) produced by physical vapor-deposited (PVD).[51] In MNCFs, the T_g is increased by ~30 K upon confinement, resulting in much slower dynamics at room temperature. In PVD glasses of IMC, under optimal deposition conditions, the fictive temperature is decreased by $\sim$ 30 K,[51,61] also resulting in an effective increase in the film's relaxation times at room temperature, to a similar degree. Under UV irradiation in inert conditions, the rate of degradation in IMC SGs is ~1.3% times slower than that of the liquid-quenched glass (analogous to the pure IMC films reported here). This is only a moderate improvement compared to the more than 6 decades of slow-down of the photodegradation rate in confinement. In addition, MNCFs establish both thermal stability and photostability for the small organic molecules,[27,62–64] while stable glasses readily transform upon heating above T_g, with only $\sim$ 17 K increase in their thermal transformation onset.[51,61] As such, vapor-deposited glasses are in their supercooled liquid state at temperatures relevant to thermal degradation. Moreover, MNCFs can be easily produced using a large combination of molecules and NPs, providing an immense

opportunity for design.

Conclusions

In summary, we studied the thermal stability and photostability of indomethacin confined in nanoporous silica nanoparticle films with diameters ranging from 11 nm to 100 nm. Under the inert conditions used in this study, IMC degrades primarily through decarboxylation, which requires the diffusion of CO_2 products out of the nanoporous films. As the NP diameter is decreased, the loss of configurational entropy and increased interactions of IMC with silica surface result in an increase in T_g (by $\sim$ 30 K in 11 nm NPs) and slower gas diffusion. As a result, after the degradation of the free surface region ($\sim$ 1 NP diameter), the diffusion-limited thermal degradation of IMC slows down dramatically. The activation energy for thermal degradation increases by as much as $\sim$70 kJ/mol in 11 nm NPs. The extreme confinement effects on photodegradation are much more dramatic. In the solid state, in addition to slow diffusion, the decarboxylation of IMC requires volume relaxation of the remaining material, which is hindered by the rigid NP scaffold. These effective (N,V,T) conditions further reduce the rate of photodegradation, an entropy-increasing reaction, due to Le Chatelier's principle. As such, after the degradation of the free surface region, no further degradation is observed within the time scale of the experiments. We note that these observations can likely extended to other diffusion-limited and entropy-increasing reactions under extreme confinement. However, extrapolation to other reactions may require careful experimental investigation. The utilization of extreme nanoconfinement as a general approach to enhance material stability under harsh conditions can greatly enhance the design of multi-functional coatings made of polymers and molecular glasses for various applications.

Supporting Information

Additional SE modeling and data, calculation of the porosity of the NP films, and detailed experimental procedures can be found in Supporting Information.

Data Availability

All data supporting the findings in this study are available via Figshare at https://doi.org/10.6084/m9.figshare.26609881.

Acknowledgements

This work is supported by the funding sources National Science Foundation (NSF) Graduate Research Fellowship Program (GRFP) (DGE-1845298). Authors acknowledge partial funding through the University of Pennsylvania Materials Research Science and Engineering Center (MRSEC) (DMR-1720530) and Wisconsin MRSEC grant (DMR-2309043). A.A.S. was supported with a postdoctoral fellowship from the Vagelos Institute of Energy Science and Technology (VIEST). We thank Prof. Thomas Mallouk's lab for the spectrophotometer and Dr. Langqiu Xiao for helping with data collection.

References

(1) Zhuge, J.; Gou, J.; Ibeh, C. Flame Resistant Performance of Nanocomposites Coated with Exfoliated Graphite Nanoplatelets/Carbon Nanofiber Hybrid Nanopapers. *Fire and Materials* **2012**, *36*, 241–253.

(2) Tjong, S. C. Structural and Mechanical Properties of Polymer Nanocomposites. *Materials Science and Engineering: R: Report* **2006**, *53*, 73–197.

(3) Musbah, S. S.; Radojevic, V. J.; Borna, N. V.; Stojanovic, D. B.; Dramicanin, M. D.; Marinkovic, A. D.; Aleksic, R. R. PMMA-Y_2O_3 (Eu^{3+}) Nanocomposites: Optical and Mechanical Properties. *Journal of the Serbian Chemical Society* **2011**, *76*, 1153–1161.

(4) Bao, W. S.; Meguid, S. A.; Zhu, Z. H.; Pan, Y.; Weng, G. J. A Novel Approach to Predict the Electrical Conductivity of Multifunctional Nanocomposites. *Mechanics of Materials* **2012**, *46*, 129–138.

(5) Huang, X.; Sun, B.; Zhu, Y.; Li, S.; Jiang, P. High-k Polymer Nanocomposites with 1D Filler for Dielectric and Energy Storage Applications. *Progress in Materials Science* **2019**, *100*, 187–225.

(6) Liu, J.; Hui, D.; Lau, D. Two-dimensional nanomaterial-based polymer composites: Fundamentals and applications. *Nanotechnology Reviews* **2022**, *11*, 770–792.

(7) Chen, G.; Seo, J.; Yang, C.; Prasad, P. N. Nanochemistry and Nanomaterials for Photovoltaics. *Chemical Society Reviews* **2013**, *42*, 8304–8338.

(8) Topolniak, I.; Chapel, A.; Gaume, J.; Bussiere, P.-O.; Chadeyron, G.; Gardette, J.-L.; Therias, S. Applications of Polymer Nanocomposites as Encapsulants for Solar Cells and LEDs: Impact of Photodegradation on Barrier and Optical Properties. *Polymer Degradation and Stability* **2017**, *145*, 52–59.

(9) Godovsky, D. In *Biopolymers/PVA Hydrogels/Anionic Polymerisation Naocomposites*; Abe, A, Ed.; Advances in Polymer Science; 2000; Vol. 153; pp 163–205.

(10) Idumah, C. I.; Obele, C. M.; Emmanuel, E. O.; Hassan, A. Recently Emerging Nanotechnological Advancements in Polymer Nanocomposite Coatings for Anti-corrosion, Anti-fouling and Self-healing. *Surfaces and Interfaces* **2020**, *21*, 100734.

(11) Khdary, N. H.; Abdelsalam, M. E. Polymer-Silica Nanocomposite Membranes for CO_2 Capturing. *Arabian Journal of Chemistry* **2020**, *13*, 557–567.

(12) Jouault, N.; Zhao, D.; Kumar, S. K. Role of Casting Solvent on Nanoparticle Dispersion in Polymer Nanocomposites. *Macromolecules* **2014**, *47*, 5246–5255.

(13) Laachachi, A.; Leroy, E.; Cochez, M.; Ferriol, M.; Cuesta, J. Use of Oxide Nanoparticles and Organoclays to Improve Thermal Stability and Fire Retardancy of Poly(methyl methacrylate). *Polymer Degradation and Stability* **2005**, *89*, 344–352.

(14) Bera, O.; Pilić, B.; Pavličević, J.; Jovičić, M.; Holló, B.; Mészáros Szécsényi, K.; Špírková, M. Preparation and Thermal Properties of Polystyrene/Silica Nanocomposites. *Thermochimica Acta* **2011**, *515*, 1–5.

(15) Moll, J.; Kumar, S. K. Glass Transitions in Highly Attractive Highly Filled Polymer Nanocomposites. *Macromolecules* **2012**, *45*, 1131–1135.

(16) Chrissafis, K.; Bikiaris, D. N. Can Nanoparticles Really Enhance Thermal Stability of Polymers? Part I: An Overview on Thermal Decomposition of Addition Polymers. *Thermochimica Acta* **2011**, *523*, 25–45.

(17) Bourbigot, S.; Gilman, J.; Wilkie, C.; Bourbigot, S.; Gilman, J. W.; Wilkie, C. A. Kinetic Analysis of the Thermal Degradation of Polystyrene–Montmorillonite Nanocomposite. *Polymer Degradation and Stability* **2004**, *84*, 483–492.

(18) Vaziri, H.; Omaraei, I.; Yousefi, N.; Vaziri, H. S.; Omaraei, I. A.; Abadyan, M.; Mortezaei, M.; Yousefi, N. Thermophysical and Rheological Behavior of Polystyrene/Silica Nanocomposites: Investigation of Nanoparticle Content. *Materials and Design* **2011**, *32*, 4537–4542.

(19) Lu, S.; Rodrigues, R.; Huang, S.; Estabrook, D.; Chapman, J.; Guan, X.; Sletten, E. M.; Liu, C. Perfluorocarbon Nanoemulsions Create A Beneficial O_2 Microenvironment in N_2-Fixing Biological | Inorganic Hybrid. *Chem Catalysis* **2021**, *1*, 704–720.

(20) Weizman, O.; Mead, J.; Dodiuk, H.; Ophir, A.; Kenig, S. The Effect of Nanoparticles on the Loss of UV Stabilizers in Polyethylene Films. *Polymer Degradation and Stability* **2022**, *195*, 109811.

(21) Zhao, H.; Sen, S.; Udayabhaskararao, T.; Sawczyk, M.; Kučanda, K.; Manna, D.; Kundu, P. K.; Lee, J.-W.; Král, P.; Klajn, R. Reversible Trapping and Reaction Acceleration within Dynamically Self-Assembling Nanoflasks. *Nature Nanotechnology.* **2016**, *11*, 82–88.

(22) Zhao, H.; Simon, S. L. Methyl Methacrylate Polymerization in Nanoporous Confinement. *Polymer: the International Journal for the Science and Technology of Polymers.* **2011**, *52*, 4093–4098.

(23) Alexandris, S.; Papadopoulos, P.; Sakellariou, G.; Steinhart, M.; Butt, H.-J.; Floudas, G. Interfacial Energy and Glass Temperature of Polymers Confined to Nanoporous Alumina. *Macromolecules* **2016**, *49*, 7400–7414.

(24) Alcoutlabi, M.; McKenna, G. B. Effects of Confinement on Material Behaviour at the Nanometre Size Scale. *Journal of Physics: Condensed Matter* **2005**, *17*, R461.

(25) Jackson, C. L.; McKenna, G. B. The Glass Transition of Organic Liquids Confined to Small Pores. *Journal of Non-crystalline Solids* **1991**, 221–224.

(26) Wang, H.; Kearns, K. L.; Zhang, A.; Shamsabadi, A. A.; Jin, Y.; Bond, A.; Hurney, S. M.; Morillo, C.; Fakhraai, Z. Effect of Nanopore Geometry in the Conformation and Vibrational Dynamics of a Highly Confined Molecular Glass. *Nano Letters* **2021**, *21*, 1778–1784.

(27) Bari, R.; Denton, A. A.; Fondren, Z. T.; McKenna, G. B.; Simon, S. L. Acceleration of Decomposition of CL-20 Explosive under Nanoconfinement. *Journal of Thermal Analysis and Calorimetry* **2020**, *140*, 2649–2655.

(28) Blaszczyk-Lezak, I.; Maiz, J.; Sacristán, J.; Mijangos, C. Monitoring the Thermal Elimination of Infiltrated Polymer from AAO Templates: An Exhaustive Characterization after Polymer Extraction. *Industrial and Engineering Chemistry Research* **2011**, *50*, 10883–10888.

(29) Huang, Y.-R.; Jiang, Y.; Hor, J. L.; Gupta, R.; Zhang, L.; Stebe, K. J.; Feng, G.; Turner, K. T.; Lee, D. Polymer Nanocomposite Films with Extremely High Nanoparticle Loadings via Capillary Rise Infiltration (CaRI). *Nanoscale* **2015**, *7*, 798–805.

(30) Hor, J. L.; Jiang, Y.; Ring, D. J.; Riggleman, R. A.; Turner, K. T.; Lee, D. Nanoporous Polymer-Infiltrated Nanoparticle Films with Uniform or Graded Porosity via Undersaturated Capillary Rise Infiltration. *ACS Nano* **2017**, *11*, 3229–3236.

(31) Wang, H.; Hor, J. L.; Zhang, Y.; Liu, T.; Lee, D.; Fakhraai, Z. Dramatic Increase in Polymer Glass Transition Temperature under Extreme Nanoconfinement in Weakly Interacting Nanoparticle Films. *ACS Nano* **2018**, *12*, 5580–5587.

(32) Wang, H.; Qiang, Y.; Shamsabadi, A. A.; Mazumder, P.; Turner, K. T.; Lee, D.; Fakhraai, Z. Thermal Degradation of Polystyrene under Extreme Nanoconfinement. *ACS Macro Letters* **2019**, *8*, 1413–1418.

(33) Hor, J. L.; Wang, H.; Fakhraai, Z.; Lee, D. Effect of Polymer-Nanoparticle Interactions on the Viscosity of Unentangled Polymers under Extreme Nanoconfinement during Capillary Rise Infiltration. *Soft Matter* **2018**, *14*, 2438–2446.

(34) Jiang, Y.; Hor, J. L.; Lee, D.; Turner, K. T. Toughening Nanoparticle Films via Polymer Infiltration and Confinement. *ACS Applied Materials and interfaces.* **2018**, *10*, 44011–44017.

(35) Qiang, Y.; Pande, S. S.; Lee, D.; Turner, K. T. The Interplay of Polymer Bridging and Entanglement in Toughening Polymer-Infiltrated Nanoparticle Films. *ACS Nano* **2022**, *16*, 6372–6381.

(36) Jin, D.; Zhong, J. Melting Point of a Confined Fluid within Nanopores: The Composition Effect on the Gibbs–Thomson Equation. *The Journal of Physical Chemistry B* **2023**, *127*, 5295–5307.

(37) Kaptay, G. The Gibbs equation versus the Kelvin and the Gibbs-Thomson equations to describe nucleation and equilibrium of nano-materials. *Journal of nanoscience and nanotechnology* **2012**, *12*, 2625–2633.

(38) Han, T.-H.; Choi, M.-R.; Jeon, C.-W.; Kim, Y.-H.; Kwon, S.-K.; Lee, T.-W. Ultrahigh-Efficiency Solution-Processed Simplified Small-Molecule Organic Light-Emitting Diodes Using Universal Host Materials. *Science Advances* **2016**, *2*, e1601428.

(39) Huang, Q.; Cui, J.; Veinot, J. G. C.; Yan, H.; Marks, T. J. Realization of High-Efficiency/High-Luminance Small-Molecule Organic Light-Emitting Diodes: Synergistic Effects of Siloxane Anode Functionalization/Hole-Injection Layers, and Hole/Exciton-Blocking/Electron-Transport Layers. *Applied Physics Letters* **2003**, *82*, 331–333.

(40) Chopra, K. L.; Paulson, P. D.; Dutta, V. Thin-Film Solar Cells: An Overview. *Progress in Photovoltaics: Research and Applications* **2004**, *12*, 69–92.

(41) Suzuki, T.; Kitamura, S.; Khota, R.; Sugihara, K.; Fujimoto, N.; Ohta, S. Estrogenic and Antiandrogenic Activities of 17 Benzophenone Derivatives Used as UV Stabilizers and Sunscreens. *Toxicology and Applied Pharmacology.* **2005**, *203*, 9–17.

(42) Luo, P.; Wolf, S. E.; Govind, S.; Stephens, R. B.; Kim, D. H.; Chen, C. Y.; Nguyen, T.; Wąsik, P.; Zhernenkov, M.; Mcclimon, B.; others High-density stable glasses formed on soft substrates. *Nature Materials* **2024**, *23*, 688–694.

(43) Jin, Y.; Zhang, A.; Wolf, S. E.; Govind, S.; Moore, A. R.; Zhernenkov, M.; Freychet, G.; Arabi Shamsabadi, A.; Fakhraai, Z. Glasses denser than the supercooled liquid. *Proceedings of the National Academy of Sciences* **2021**, *118*, e2100738118.

(44) Zhang, A.; Moore, A. R.; Zhao, H.; Govind, S.; Wolf, S. E.; Jin, Y.; Walsh, P. J.; Riggleman, R. A.; Fakhraai, Z. The role of intramolecular relaxations on the structure and stability of vapor-deposited glasses. *The Journal of chemical physics* **2022**, *156*, 244703.

(45) Baklanov, b. M.; Mogilnikov, K.; Polovinkin, V.; Dultsev, F. Determination of pore size distribution in thin films by ellipsometric porosimetry. *Journal of Vacuum Science & Technology B: Microelectronics and Nanometer Structures Processing, Measurement, and Phenomena* **2000**, *18*, 1385–1391.

(46) Kim, B. Q.; Füredi, M.; Venkatesh, R. B.; Guldin, S.; Lee, D. Water-Induced Separation of Polymers from High Nanoparticle-Content Nanocomposite Films. *Small* **2023**, *19*, 2302676.

(47) Song, B.; Liu, F.; Wang, H.; Miao, J.; Chen, Y.; Kumar, P.; Zhang, H.; Liu, X.; Gu, H.; Stach, E. A.; others Giant gate-tunability of complex refractive index in semiconducting carbon nanotubes. *ACS Photonics* **2020**, *7*, 2896–2905.

(48) Lynch, J.; Smith, E.; Alfieri, A.; Song, B.; Klein, M.; Stevens, C. E.; Chen, C. Y.; Lawrence, C. F.; Kagan, C. R.; Gu, H.; others Gate-tunable optical anisotropy in wafer-scale, aligned carbon nanotube films. *Nature Photonics* **2024**, *18*, 1176–1184.

(49) Shamsabadi, A. A.; Fang, H.; Zhang, D.; Thakur, A.; Chen, C. Y.; Zhang, A.; Wang, H.; Anasori, B.; Soroush, M.; Gogotsi, Y.; others The evolution of MXenes conductivity and optical properties upon heating in air. *Small methods* **2023**, *7*, 2300568.

(50) Shimada, Y.; Komaki, H.; Hirai, A.; Goto, S.; Hashimoto, Y.; Uchiro, H.; Terada, H. Decarboxylation of Indomethacin Induced by Heat Treatment. *International Journal of Pharmaceutics* **2018**, *545*, 51–56.

(51) Qiu, Y.; Dalal, S. S.; Ediger, M. D. Vapor-Deposited Organic Glasses Exhibit Enhanced Stability against Photodegradation. *Soft Matter* **2018**, *14*, 2827–2834.

(52) Manohar, N.; Stebe, K. J.; Lee, D. Solvent-Driven Infiltration of Polymer (SIP) into Nanoparticle Packings. *ACS Macro Letters* **2017**, *6*, 1104–1108, PMID: 35650925.

(53) Herzinger, C. M.; Johs, B.; McGahan, W. A.; Woollam, J. A.; Paulson, W. Ellipsometric Determination of Optical Constants for Silicon and Thermally Grown Silicon Dioxide via A Multi-Sample, Multi-Wavelength, Multi-Angle Investigation. *Journal of Applied Physics* **1998**, *83*, 3323–3336.

(54) Bertei, A.; Nucci, B.; Nicolella, C. Effective Transport Properties in Random Packings of Spheres and Agglomerates. *Chemical Engineering Transactions* **2013**, *32*, 1531–1536.

(55) Dullien, F. A. *Porous media: fluid transport and pore structure*; Academic press, 2012.

(56) Ediger, M. D.; Angell, C. A.; Nagel, S. R. Supercooled Liquids and Glasses. *The Journal of Physical Chemistry* **1996**, *100*, 13200–13212.

(57) Zhang, Y.; Glor, E. C.; Li, M.; Liu, T.; Wahid, K.; Zhang, W.; Riggleman, R. A.; Fakhraai, Z. Long-Range Correlated Dynamics in Ultra-Thin Molecular Glass Films. *The Journal of Chemical Physics* **2016**, *145*, 114502.

(58) Shi, Y.; Liu, C.; Liu, L.; Fu, L.; Yu, B.; Lv, Y.; Yang, F.; Song, P. Strengthening, Toughing and Thermally Stable Ultra-Thin MXene Nanosheets/Polypropylene Nanocomposites via Nanoconfinement. *Chemical Engineering Journal* **2019**, *378*, 122267.

(59) Pavlicevic, J.; Spirkova, M.; Jovicic, M.; Budinski-Simendic, J.; Pilic, B.; Balos, S.; Bera, O. Structure-Functional Property Relationship of Aliphatic Polyurethane-Silica Hybrid Films. *Progress in Organic Coatings* **2019**, *126*, 62–74.

(60) Jelić, D.; Liavitskaya, T.; Vyazovkin, S. Thermal Stability of Indomethacin Increases with the Amount of Polyvinylpyrrolidone in Solid Dispersion. *Thermochimica Acta* **2019**, *676*, 172–176.

(61) Dalal, S. S.; Ediger, M. D. Molecular orientation in stable glasses of indomethacin. *The journal of physical chemistry letters* **2012**, *3*, 1229–1233.

(62) Zapata, J. A.; Simon, S. L.; Grady, B. P. Influence of Diameter on the Degradation Profile of Multiwall Carbon Nanotubes. *Journal of Thermal Analysis and Calorimetry* **2019**, *138*, 1351–1362.

(63) Zhang, Q.; Gu, Q.; Leroux, F.; Tang, P.; Li, D.; Feng, Y. Co-intercalated layered double hydroxides as thermal and photo-oxidation stabilizers for polypropylene. *Beilstein Journal of Nanotechnology* **2018**, *9*, 2980–2988.

(64) Qin, S.; Pour, M. G.; Lazar, S.; Köklükaya, O.; Gerringer, J.; Song, Y.; Wågberg, L.; Grunlan, J. C. Super Gas Barrier and Fire Resistance of Nanoplatelet/Nanofibril Multilayer Thin Films. *Advanced Materials Interfaces* **2019**, *6*, 1801424.

TOC Graphic

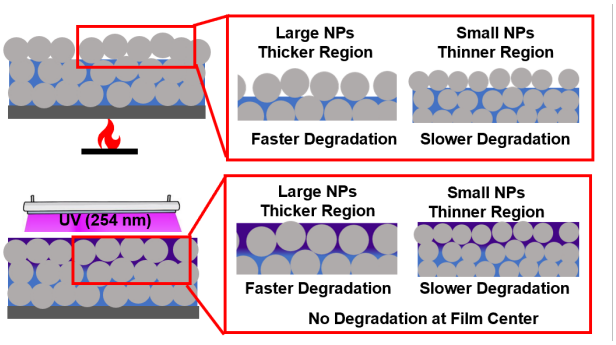
Large NPs
Thicker Region
Small NPs
Thinner Region
Faster Degradation
Slower Degradation
UV (254 nm)
Large NPs
Thicker Region
Small NPs
Thinner Region
Faster Degradation
Slower Degradation
No Degradation at Film Center